nature communications

Article

https://doi.org/10.1038/s41467-025-67839-6

Two-Dimensional Metastable-Phase Nickel Hexagonal Nanosheets for Highly-Performance Electrochemical Acetone Hydrogenation

Received: 26 May 2025

Accepted: 8 December 2025

Long Chen[1], Zonghao Zhang[2], Penghao Li[2], Hanzhuo Luo[1], Chenchen Li[1], Sihui Pan[2], Wei-Hsiang Huang[3,4], Chih-Wen Pao[3], Hao Yang[2], Zhiwei Hu[5] & Qi Shao[1] ✉

Electrocatalytic acetone hydrogenation into high-value alcohols offers a sustainable alternative to thermal methods. However, developing non-noble metal catalysts with superior performance for electrocatalytic acetone hydrogenation remains challenging. Two-dimensional non-noble metal structure with metastable-phase active sites is promising due to its high-energy structure and unique electronic environment. However, its precise synthesis remains a great challenge. In this work, we report a two-dimensional metastable hexagonal close-packed phase nickel nanosheets (hcp Ni NSs) with a space group of $P6_3/mmc$. In the electrocatalytic acetone hydrogenation, it achieves 95.0 % acetone conversion with 100 % isopropanol selectivity. Notably, in the scale-up experiment, the hcp Ni NSs also exhibit 11.51 $g\,g_{cat}^{-1}\,h^{-1}$ isopropanol production rate at a current density of −250 $mA\,cm^{-2}$. Furthermore, this catalyst is widely applicable to various carbonyl compounds. Mechanism study shows that hcp Ni NSs enable strong acetone adsorption and rapid isopropanol desorption.

As the demand for renewable energy and sustainable chemicals continues to increase, finding efficient and environmentally friendly catalysts has become one of the important challenges in today's chemistry. Selective hydrogenation has been shown to be an economical and environmentally compatible synthetic method for the preparation of various fine chemicals[1–6]. Acetone catalytic hydrogenation is widely used in the manufacture of fine chemicals and the refining of biomass-derived compounds. So far, a variety of metal catalysts for acetone selective hydrogenation to prepare isopropanol have been reported[7–10]. However, they are mainly based on traditional thermal catalytic hydrogenation, using explosive hydrogen or other hydrogen donors (e.g., HCOOH, $NaBH_4$) as hydrogen sources[11–15], which lead to high energy consumption, high cost and serious safety problems.

Electrocatalytic hydrogenation (ECH) provides a green and environmentally friendly route for catalytic hydrogenation[16–19]. Yet, it is often accompanied by the more kinetically favourable hydrogen evolution reaction, resulting in unsatisfactory conversion and selectivity of ECH. Therefore, the rational design of catalysts with high activity, selectivity and stability has attracted extensive attention. Nickel (Ni), as the fourth most abundant transition metal on earth, is considered as a potential candidate to replace precious metal catalysts such as Pt and Pd[20–24], however, its activity for electrocatalytic hydrogenation remains unsatisfactory. Compared with the stable-phase, two-dimensional (2D) metastable-phase catalysts exhibit high catalytic activity due to their large specific surface area, high-energy structure and unique electronic

---

[1]College of Chemistry, Chemical Engineering and Materials Science, Soochow University, Jiangsu 215123, China. [2]Institute of Functional Nano and Soft Materials (FUNSOM), Soochow University, Jiangsu 215123, China. [3]National Synchrotron Radiation Research Center (NSRRC), Hsinchu 300092, Taiwan. [4]Sustainable Electrochemical Energy Development (SEED) Center, National Taiwan University of Science and Technology, Taipei 106, Taiwan. [5]Max-Planck-Institute for Chemical Physics of Solids, Nöthnitzer Street 40, Dresden 01187, Germany. ✉e-mail: qshao@suda.edu.cn

environment[25–31], making them promising candidates to solve this problem.

In this work, we report a two-dimensional metastable hexagonal close-packed (hcp) phase Ni hexagonal nanosheets (NSs) catalyst with a space group of $P6_3/mmc$. The hcp Ni NSs exhibit high performance in the electrocatalytic acetone hydrogenation to isopropanol, which has 95.0 % acetone conversion (con.) with 100 % isopropanol selectivity (sel.), much higher than fcc Ni NPs (con.: 51.0 %, sel.: 100 %) (Fig. 1). Notably, in the scale-up experiment, the hcp Ni NSs exhibited acetone conversion of 95.9 % with isopropanol selectivity of 100 % and isopropanol production rate of 11.51 g g_{cat}^{-1} h^{-1} at a current density of −250 mA cm^{-2}. Furthermore, this catalyst remains at around 80% acetone conversion after thirty cycles of testing at −1.32 V vs. reversible hydrogen electrode (RHE) and is widely applicable to various carbonyl compounds.

Results

Synthesis and structural characterizations of hcp Ni hexagonal nanosheets

The hcp Ni NSs was successfully fabricated by a one-pot method using bis (η5-2,4-cyclopentadien-1-yl) nickel as a precursor, glucose as a reducing agent, formaldehyde as a surfactant, and oleylamine as a solvent, as illustrated in Fig. 2a. The phase of hcp Ni NSs was identified by powder X-ray diffraction (XRD). As shown in Fig. 2b, the diffraction peaks of hcp Ni NSs can be clearly attributed to the hcp Ni phase (JCPDS No. 45-1027, $P6_3/mmc$), while there is no face-centered cubic (fcc) Ni phase (JCPDS No. 04-0850, Fm-3m)[32], indicating the high purity of the metastable hcp phase Ni. Low-magnification transmission electron microscopy (TEM) images showed the sheet-like morphology of hcp Ni NSs (Fig. 2c, f). TEM image shows that hcp Ni NSs has a two-dimensional hexagonal nanosheets morphology with the side length of 21.9 ± 0.5 nm and the diameter of 33.6 ± 0.4 nm (Fig. 2d, e). Moreover, zoom-in side-view TEM image demonstrated the thickness of the two-dimensional hexagonal nanosheets is 6.9 nm (Fig. 2f). The high-resolution transmission electron microscopy (HRTEM) image displays the fringe patterns showing the presence of the (01-10) plane of hcp Ni NSs (Fig. 2g, h, i). Figure 2i and Fig. 2j clearly reveal the crystal structure of hcp Ni NSs. Corresponding Fourier diffractogram (FD) patterns framed by dotted lines further confirms the hexagonal lattice of hcp Ni NSs (the inset of Fig. 2h). The lattice spacing framed by dotted lines in Fig. 2i was measured as 0.23 nm (Fig. 2k), corresponding to the (10-10) and (01-10) crystal planes. Moreover, we also synthesized hcp Ni NPs (JCPDS No. 45-1027, $P6_3/mmc$) (Fig. 2b and Supplementary Fig. 1) and fcc Ni NPs (JCPDS No. 04-0850, Fm-3m) (Fig. 2b and Supplementary Fig. 2) as comparative materials.

The synthesis of metastable-phase material is a kinetic-controlled process and the reducibility of different precursors is crucial for controlling the morphology. As shown in Supplementary Figs. 3, 4, when using other nickel precursors such as nickel acetylacetonate ($Ni(acac)_2$), nickel (II) formate ($Ni(HCO_2)_2{\cdot}2H_2O$), nickel oxalate dihydrate ($NiC_2O_4{\cdot}2H_2O$) and bis (triphenylphosphine) nickel (II) bromide ($NiBr_2(PPh_3)_2$), the crystallinity of hcp Ni was weak and even hcp Ni cannot be synthesized (Supplementary Figs. 3, 4). Therefore, bis (η5-2,4-cyclopentadien-1-yl) nickel was used to synthesize hcp Ni hexagonal nanosheets. Glucose is important to form the hcp Ni. When other sugar compounds such as fructose and ribose were used as reducing agents, the characteristic diffraction peaks of nickel hydroxide ($Ni(OH)_2$) and metastable phase hcp Ni both appeared (Supplementary Fig. 5a, b). In addition, when phenol is used as a reducing agent, only stable phase fcc Ni can be synthesized (Supplementary Fig. 5c). Formaldehyde, as a morphology regulator, releases CO during heating, which can promote the growth of two-dimensional hexagonal nanosheets. When reducing the amount of formaldehyde, the hcp Ni tends to grow toward a nanoparticle morphology (Supplementary Fig. 6). To explore the formation process of hcp Ni NSs specifically, the samples obtained at different reaction times were characterized respectively (Supplementary Figs. 7-8). At reaction time of 15 minutes, the amorphous nanosheets were synthesized (Supplementary Figs. 7a, 8a). After 90 minutes of continuous reaction, the amorphous nanosheets were gradually disappear with hexagonal sheets appear (Supplementary Fig. 7e), and the characteristic diffraction peaks of nickel hydroxide and metastable hcp

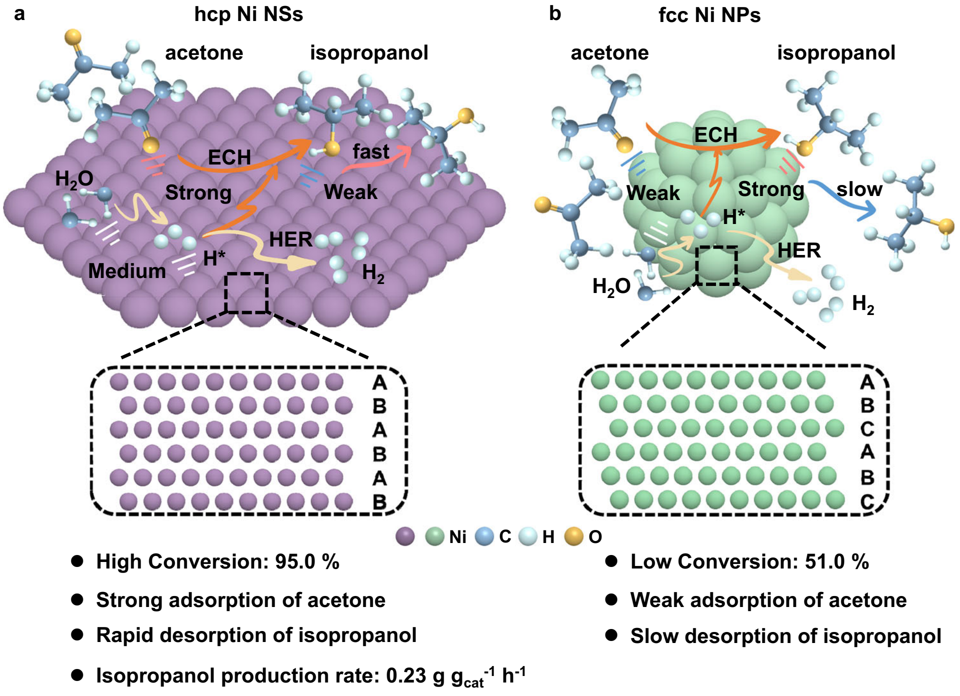

Fig. 1 | Enhancing electrocatalytic acetone hydrogenation performance through morphology and crystal phase regulation strategy. **a** A high acetone conversion and isopropanol production rate due to strong adsorption of acetone and rapid desorption of isopropanol on hcp Ni NSs. **b** A low acetone conversion caused by weak adsorption of acetone and slow desorption of isopropanol on fcc Ni NPs.

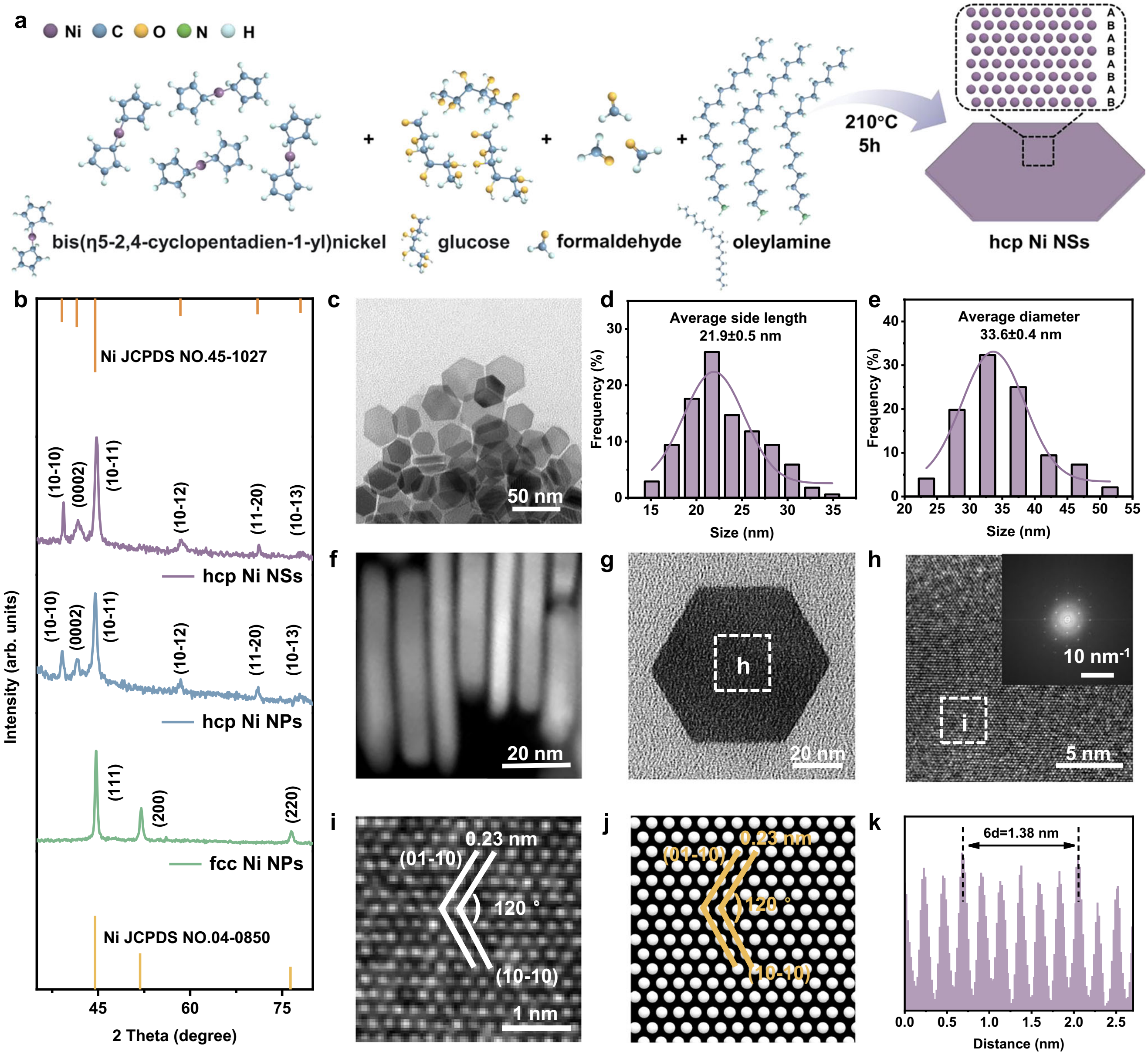

Fig. 2 | Structural characterizations of hcp Ni NSs. a Schematic diagram of the synthesis of hcp Ni NSs. **b** XRD patterns of hcp Ni NSs, hcp Ni NPs and fcc Ni NPs. **c** Low-magnification TEM of hcp Ni NSs. **d** Average side length of hcp Ni NSs. **e** Average diameter of hcp Ni NSs. **f** Zoom-in side-view HAADF-STEM image of hcp Ni NSs. **g** High-magnification TEM image of hcp Ni NSs. **h** HRTEM image of hcp Ni NSs in (**g**) and FD pattern (inset). **i** Enlarged HRTEM image of hcp Ni NSs in (**h**). **j** Simulated HRTEM image of (**i**). (**k**) The lattice fringe spacing corresponding to the areas labeled as h in (**i**).

phase Ni appeared (Supplementary Fig. 8e). When the reaction time was extended to 120 minutes, the characteristic peaks of nickel hydroxide and metastable hcp phase Ni are more obvious (Supplementary Figs. 7f, 8f). When extending the reaction time, the characteristic diffraction peak of nickel hydroxide gradually disappeared. When the reaction time was 240 minutes, only the characteristic XRD peak of metastable hcp phase Ni existed, and the surface of hexagonal sheet was more flat (Supplementary Figs. 7h, 8h).

The electronic and atomic structure of hcp Ni hexagonal nanosheets

To gain insight into the local coordination environment of the catalyst, X-ray absorption near-edge structure spectroscopy (XANES) and extended X-ray absorption fine structure spectroscopy (EXAFS) were further used to conduct in-depth analysis of the electronic structure of the catalyst. Figure 3a, b show the Ni K-edge X-ray absorption near-edge spectroscopy (XANES) spectra of hcp Ni NSs, fcc Ni NPs, while NiO and Ni foil used as the references. The absorption edges at the energy positions are as follows: NiO > hcp Ni NSs > fcc Ni NPs > Ni foil, indicating that hcp Ni NSs with higher valence state[33–38]. The k3χ(k) function of the Fourier transform of the EXAFS data in the frequency domain (R) space reveals information about the coordination environment (Fig. 3c). In the EXAFS spectrum, the Ni-Ni coordination bonds of Ni foil (green dashed line in Fig. 3c) and fcc Ni NPs (blue solid line in Fig. 3c) are located at ~ 2.18 Å, and the Ni-Ni coordination bond in NiO (yellow dashed line in Fig. 3c) is located at ~ 2.59 Å. The peak at ~ 1.62 Å in NiO belongs to the Ni-O coordination[39]. The Ni-Ni coordination bond of hcp Ni NSs is ~ 2.34 Å, which is different from the Ni-Ni bond in Ni foil and fcc Ni NPs due to the different phase structure of hcp Ni NSs from fcc Ni NPs and Ni foil. Wavelet transform (WT) was used to further analyze the Ni K-edge EXAFS oscillation (Fig. 3d–f). The WT contour of hcp Ni NSs showed a maximum intensity at 7.30 $Å^{-1}$, different from the

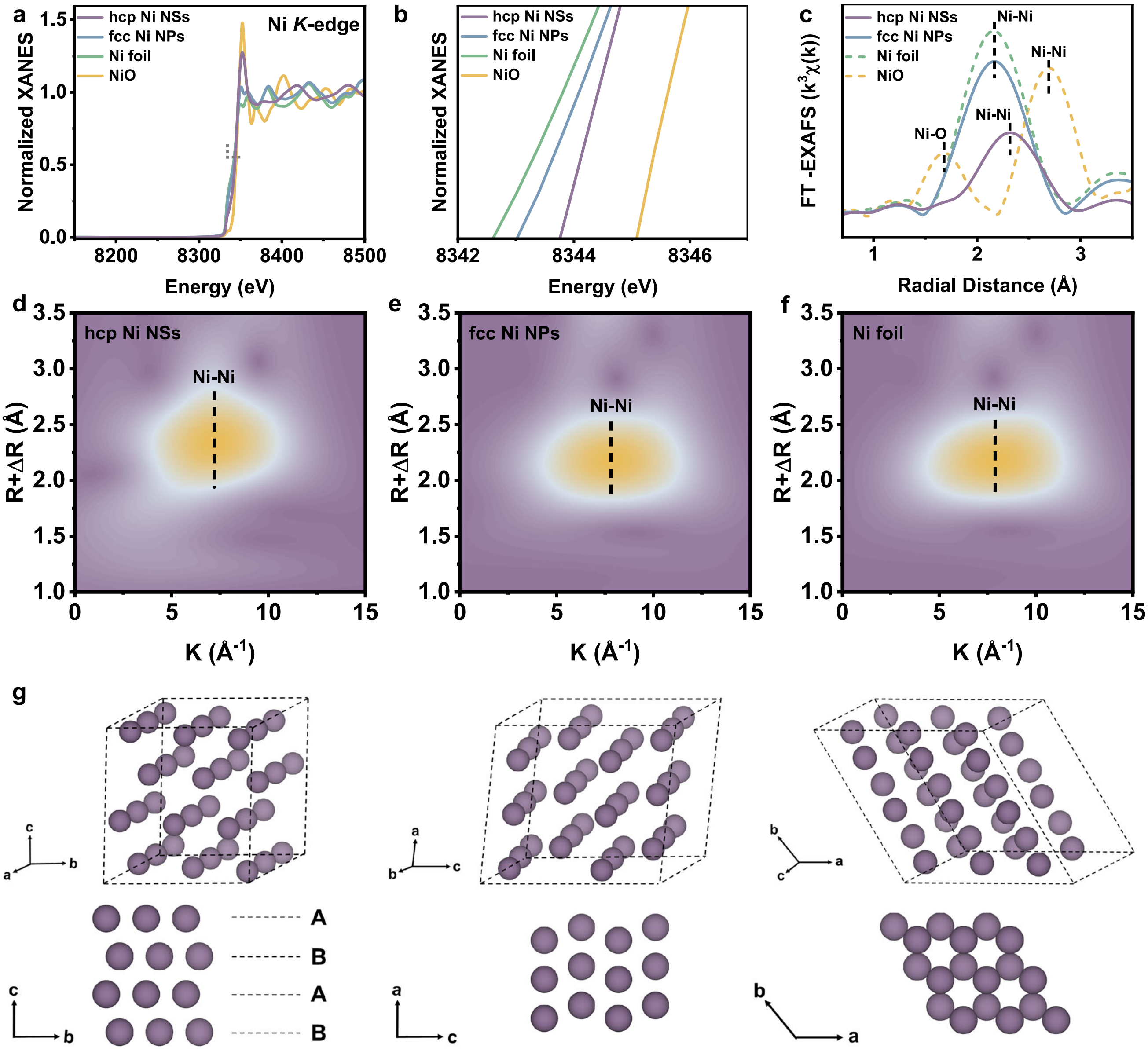

Fig. 3 | Electronic structure characterization. **a** Normalized X-ray absorption near-edge structure spectroscopy (XANES) spectra of hcp Ni NSs (purple line), fcc Ni NPs (blue line), Ni foil (green line), and NiO (yellow line) recorded at the Ni *K*-edge. **b** Enlarged view in (**a**). **c** Fourier transforms of Ni *K*-edge extended X-ray absorption fine structure spectroscopy (EXAFS) spectra of hcp Ni NSs, fcc Ni NPs, Ni foil, and NiO. **d**-**f** Wavelet transform (WT) of the k^3-weighted EXAFS at the Ni *K*-edge of hcp Ni NSs, fcc Ni NPs and Ni foil. **g** Schematic diagram of the atomic stacking model of hcp Ni NSs along **a**, **b**, and **c** directions.

maximum intensity of fcc Ni NPs (8.0 Å^{-1}) and the maximum intensity of Ni foil (8.1 Å^{-1}), which originated from Ni–Ni coordination. The results showed that hcp Ni NSs had a different coordination environment from fcc Ni NPs and Ni foil. To further highlight the differences between hcp Ni NSs and fcc Ni NPs, we analysed the crystal structure and atomic stacking of hcp Ni NSs along the a, b, and c directions, as shown in Fig. 3g. The results show that the atomic stacking of hcp Ni NSs is a typical ABAB… stacking order along the [100] direction, which is different from the ABCABC… stacking order of the stable fcc structure along the [111] direction.

Electrocatalytic hydrogenation performance of hcp Ni hexagonal nanosheets

The electrocatalytic acetone hydrogenation was chosen as a model reaction to evaluate the catalytic performance of hcp Ni NSs (Fig. 4a–d), while hcp Ni NPs (Fig. 4e–h) and fcc Ni NPs (Fig. 4i–l) were chosen as the references. The reference electrode was calibrated before the electrocatalytic testing (Supplementary Fig. 9). The reaction was carried out in a typical H-type cell by using 0.1 mmol acetone (1a) as the model substrate with 1.0 M KOH as the electrolyte (Supplementary Fig. 10). Figure 4b, f and j show the linear sweep voltammetry (LSV) curves of hcp Ni NSs, hcp Ni NPs and fcc Ni NPs in 1.0 M KOH electrolyte with/without acetone, respectively. The LSV curves are measured based on at least three independent replicates (Supplementary Fig. 11). Obviously, hcp Ni NSs, hcp Ni NPs, and fcc Ni NPs all show enhanced current densities in the presence of acetone, indicating that acetone electrocatalytic reduction prevails over the competing hydrogen evolution reaction (HER) on Ni surfaces. The optimal potential was screened by potential-dependent electrochemical experiments. The acetone conversion reached 95.0 ± 0.35% and the isopropanol selectivity was 100% at −1.32 V vs. RHE (Supplementary Fig. 12).

To further evaluate the performance of the catalyst for electrocatalytic acetone hydrogenation, we performed time-controlled

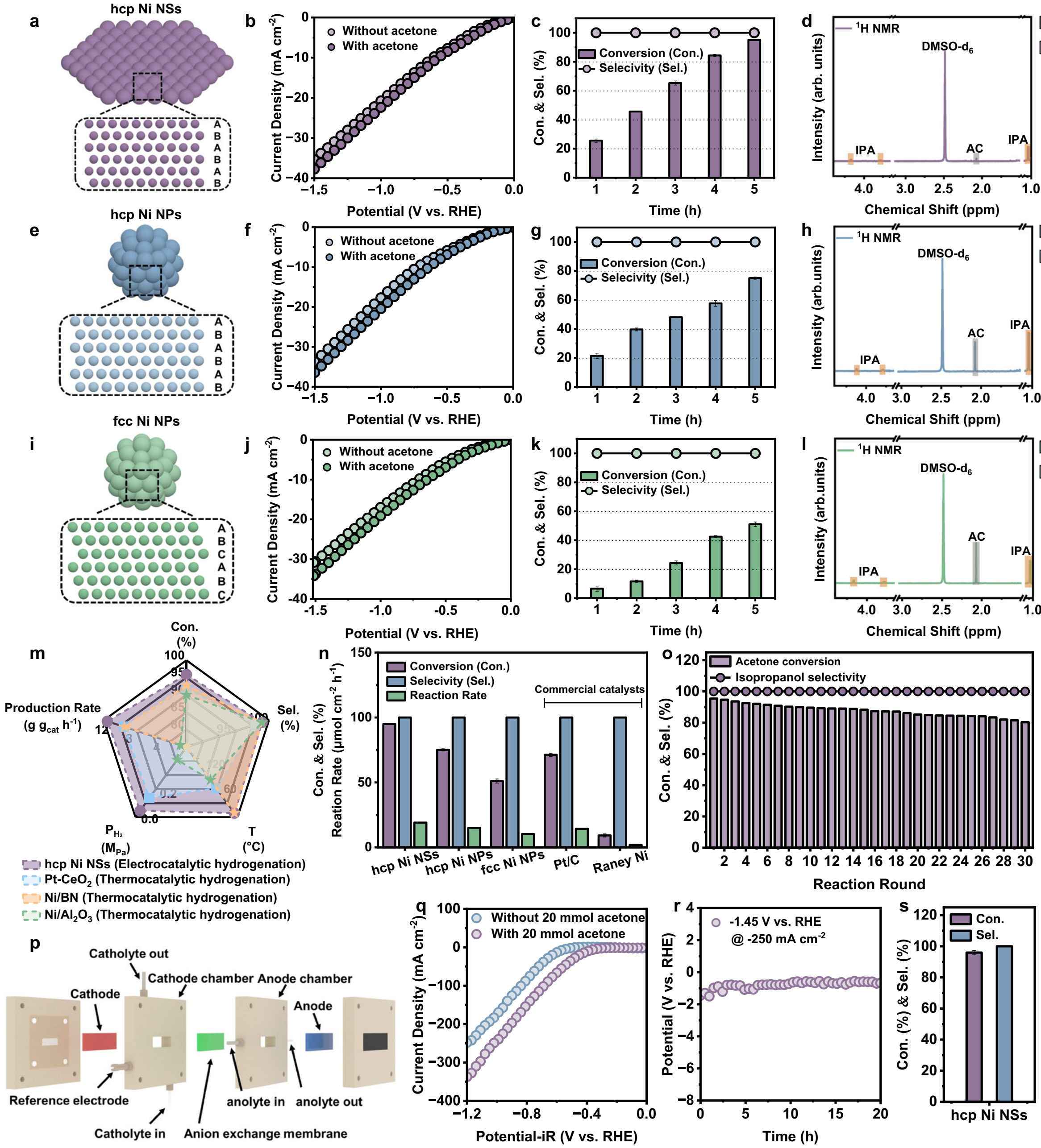

Fig. 4 | Electrochemical performance. a-l The models and electrochemical performances for acetone of **(a, b, c, d)** hcp Ni NSs, **(e, f, g, h)** hcp Ni NPs and **(i, j, k, l)** fcc Ni NPs. The yellow and gray area represent the characteristic peak position of isopropanol (IPA) and acetone (AC) respectively. Linear sweep voltammetry (LSV) was recorded without *iR* correction to obtain the polarization curves.
m Comparisons of conversion (con.), selectivity (sel.) and production rate with the reported catalysts. **n** The conversion (con.), selectivity (sel.) and reaction rate of hcp Ni NSs, hcp Ni NPs, fcc Ni NPs, commercial Pt/C and Raney Ni. **o** Catalytic stability of hcp Ni NSs. Reaction conditions: H-cell, acetone (0.1 mmol), 1.0 M KOH/H_2O electrolyte (pH=13.7 ± 0.3), scan rate: 10 mV s^{-1}, −1.32 V vs. RHE, RT, 5 h, rotation rate: 750 rpm, catalyst loading (5.0 mg cm^{-2}) and working area: 1 cm^2. **p** Schematic illustration of the flow electrolysis cell for scaled-up experiment. **q** The LSV curve of hcp Ni NSs with 95% *i*R in 1.0 M KOH/H_2O electrolyte with and without 20 mmol acetone. **r** Stability evaluation of the hcp Ni NSs at the current density of −250 mA cm^{-2}. **s** Con. and sel. of the hcp Ni NSs in 1.0 M KOH/H_2O electrolyte with 20 mmol acetone at the current density of −250 mA cm^{-2}. Reaction conditions: Flow electrolysis cell, acetone (20 mmol), 1.0 M KOH/H_2O electrolyte (pH=13.7 ± 0.3), scan rate: 10 mV s^{-1}, −250 mA cm^{-2}, RT, 20 h, catalyst loading (5.0 mg cm^{-2}) and working area: 1 cm^2. Error bars in **c, g, k, n** and **s** represent the standard deviation (SD) from three independent measurements (*n* = 3). Average (mean) values are presented. Con., conversion; sel., selectivity.

experiments at −1.32 V vs. RHE within 5 h (Supplementary Fig. 13). The results showed that hcp Ni NSs showed the largest acetone conversion in each time period (Fig. 4c). Furthermore, the acetone conversion of hcp Ni NSs and hcp Ni NPs in each time period was higher than that of fcc Ni NPs (Fig. 4c, g, k and Supplementary Fig. 13), indicating that the metastable-phase has better hydrogenation activity than the stable one. The acetone conversion is as follows: hcp Ni NSs > hcp Ni NPs > fcc Ni NPs. Quantitative analysis and verification by hydrogen nuclear magnetic resonance spectroscopy (^{1}H-NMR) show that, after 5 h of acetone electrocatalytic reduction, hcp Ni NSs, hcp Ni NPs and fcc Ni NPs showed 95.0 %, 75.1 % and 51.0 % acetone conversion, respectively, with no related by-products detected (Fig. 4d, h, l). Compared to other reported catalysts, hcp Ni NSs exhibits competitive in electrocatalytic acetone hydrogenation performance (Fig. 4m and Supplementary

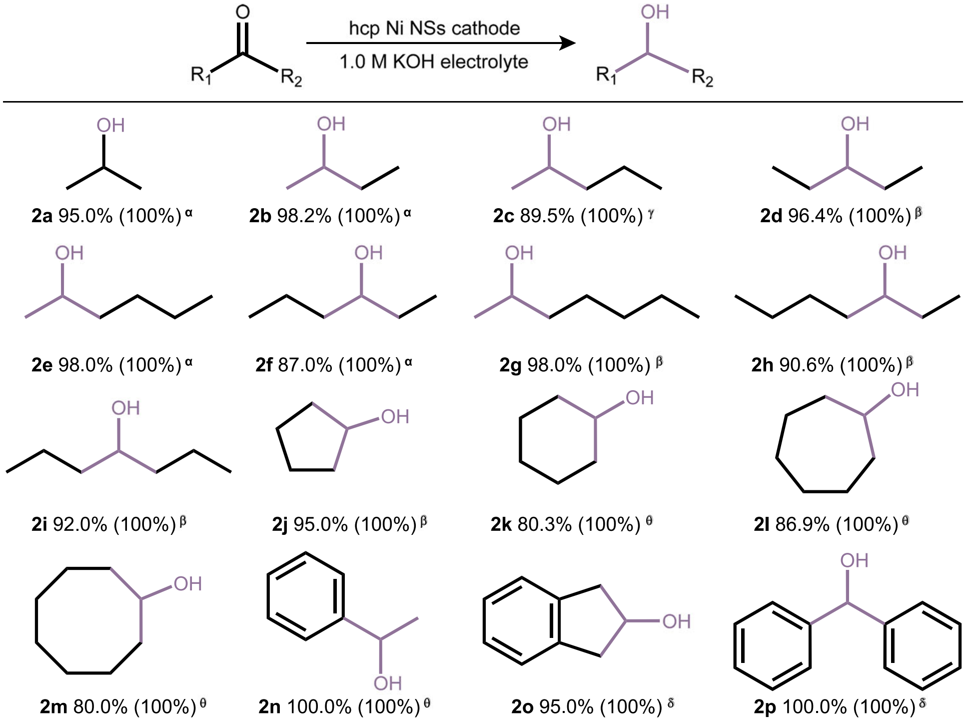

Fig. 5 | Substrate scope. Product Con. (Sel.). Reaction Conditions: H-cell, **α** substrates (0.1 mmol, 14.29 mmol L^{-1}), hcp Ni NSs electrode (working area: 1.0 cm^2), catalyst loading (5.0 mg cm^{-2}), 1.0 M KOH/H_2O electrolyte (7 mL), −1.32 V vs. RHE, RT, 5 h. **β** substrates (0.1 mmol, 14.29 mmol L^{-1}), hcp Ni NSs electrode (working area: 1.0 cm^2), catalyst loading (5.0 mg cm^{-2}), 1.0 M KOH/H_2O electrolyte (7 mL), −1.32 V vs. RHE, RT, 8 h. **γ** substrates (0.1 mmol, 14.29 mmol L^{-1}), hcp Ni NSs electrode (working area: 1.0 cm^2), catalyst loading (5.0 mg cm^{-2}), 1.0 M KOH/H_2O electrolyte (7 mL), −1.32 V vs. RHE, 50 °C, 5 h. **θ** substrates (0.1 mmol, 14.29 mmol L^{-1}), hcp Ni NSs electrode (working area: 1.0 cm^2), catalyst loading (5.0 mg cm^{-2}), 1.0 M KOH/H_2O electrolyte (7 mL), −1.32 V vs. RHE, 50 °C, 8 h. **δ** substrates (0.1 mmol, 14.29 mmol L^{-1}), hcp Ni NSs electrode (working area: 1.0 cm^2), catalyst loading (5.0 mg cm^{-2}), a mixed solvent of 1.0 M KOH/EtOH (6:1 V/V, 7 mL), −1.32 V vs. RHE, 50 °C, 8 h.

Table 1). Compared with other commercial catalysts such as Pt/C and Raney Ni, hcp Ni NSs exhibits high acetone conversion (95.0 ± 0.35%) and reaction rate (19 ± 0.07 μmol cm^{-2} h^{-1}) (Fig. 4n). In addition, hcp Ni NSs exhibits the production rate of 0.23 g g_{cat}^{-1} h^{-1}, higher than the stable one and other commercial catalysts (Supplementary Fig. 14). In addition, we investigate the effect of increasing the acetone content in the electrolyte on the acetone conversion and the Faradaic efficiency of isopropanol using hcp Ni NSs at −1.32 V vs. RHE in 5 h (Supplementary Fig. 15). The results show that adding more acetone to the electrolyte inhibits the side reaction HER and improves the Faradaic efficiency of isopropanol, but decreases the acetone conversion. Since we focused on the acetone conversion, we chose 0.1 mmol of acetone.

After electrocatalytic acetone hydrogenation reaction, hcp Ni NSs does not change the crystal phase and morphology, indicating that hcp Ni NSs is relatively stable in the reaction process (Supplementary Fig. 16). Furthermore, in order to explore the Ni valence state changes of hcp Ni NSs catalyst surface after the reaction, we performed X-ray photoelectron spectroscopy (XPS) tests on hcp Ni NSs at open circuit potential (OCP) condition and at −1.32 V vs. RHE for 5 h respectively. As observed in Ni 2*p* XPS spectra (Supplementary Fig. 17), the peak intensity of Ni-Ni bond (852.9 eV and 870.2 eV) is weakened after the reaction, indicating that the surface of the hcp Ni NSs is slightly oxidized. This may be due to the accumulation of acetone on the nickel surface and hydrogen/hydroxyl groups adsorption on hcp Ni NSs. In addition to the high reaction activity, hcp Ni NSs remains at around 80% acetone conversion after thirty cycles of testing at −1.32 V vs. RHE, As can be seen in Fig. 4o. Furthermore, the TEM image and XRD pattern show that the hexagonal sheet morphology and metastable-phase of hcp Ni NSs largely remain after the stability test (Supplementary Fig. 18).

In order to evaluate the feasibility of the catalyst for industrial application, a scale-up experiment of electrocatalytic acetone hydrogenation was carried out using a flow electrolysis cell (Fig. 4p and Supplementary Fig. 19), it is worth noting that the hcp Ni NSs exhibited 95.9 ± 1.4% acetone conversion, with 100 % isopropanol selectivity and 11.51 g g_{cat}^{-1} h^{-1} isopropanol production rate at a current density of −250 mA cm^{-2} (Fig. 4m, q, r, s). The result of ^{1}H NMR spectrum is shown in Supplementary Fig. 20.

To further characterize the electrocatalytic hydrogenation behaviour of the hcp Ni NSs catalyst, we next explored the substrate range of the ECH reaction, including aliphatic ketones, alicyclic ketones, and aromatic ketones, such as 2-butanone (**1b**), 2-pentanone (**1c**), 3-pentanone (**1d**), 2-hexanone (**1e**), 3-hexanone (**1f**), 2-heptanone (**1g**), 3-heptanone (**1h**), 4-heptanone (**1i**), cyclopentanone (**1j**), cyclohexanone (**1k**), cycloheptanone (**1l**), cyclooctenone (**1m**); acetophenone (**1n**), 2-indanone (**1o**), and benzophenone (**1p**) (Fig. 5). Considering the low solubility of some substrates in 1.0 M KOH/H_2O electrolyte, some experiments were conducted on these substrates using water-miscible organic cosolvents to eliminate the solubility limitation on their reactivity. When these ketones (**1b**–**1p**) are treated by our electrocatalytic system, the corresponding alcohol products (**2b**–**2p**) can be easily obtained. Impressively, when hcp Ni NSs were used as catalysts, the corresponding these alcohol products (**2b**–**2p**) could be readily obtained with selectivity of > 99 %, and the formation of by-products was almost undetectable. The corresponding conversions of aliphatic ketones, alicyclic ketones, and aromatic ketones were 98.2% con. of **1b**, 89.5% con. of **1c**, 96.4% con. of **1d**, 98.0% con. of **1e**, 87.0% con. of **1f**, 98.0% con. of **1g**, 90.6% con. of **1h**, 92.0% con. of **1i**, 95.0 % con. of **1j**, 80.3% con. of **1k**, 86.9% con. of **1l**, 80.0% con. of **1m**, 100.0% con. of **1n**, 95.0% con. of **1o** and 100.0% con. of **1p**, respectively (Fig. 5), with all these data being quantified and verified by ^{1}H-NMR (Supplementary

Figs. 21-37). The results suggest that hcp Ni NSs show good catalytic universality.

Mechanism exploration of electrocatalytic acetone hydrogenation

Now, it is significant to understand the catalytic mechanism. hcp Ni NSs exhibited the lowest impedance compared to hcp Ni NPs and fcc Ni NPs, which suggests that the efficient mass transfer of hcp Ni NSs (Supplementary Fig. 38). The adsorption capacity of acetone and isopropanol on hcp Ni NSs, hcp Ni NPs and fcc Ni NPs catalysts was studied by attenuated total reflection infrared spectroscopy (ATR-IR). As shown in Fig. 6a, for hcp Ni NSs and Pt/C catalysts, the strong carbonyl ($C = O$) (~ 1662.8 cm^{-1}) absorption peak of acetone can be observed, indicating that hcp Ni NSs and Pt/C have a strong adsorption capacity for acetone, which is conducive to the hydrogenation reaction, but the competitive HER reaction is prone to occur on the Pt/C surface, resulting in an unsatisfactory acetone conversion. As shown in Supplementary Fig. 39, the LSV curves of Pt/C show that the current density of the electrolyte without acetone (-32.2 mA cm^{-2}) is more negative than that of the electrolyte with acetone (-29.9 mA cm^{-2}) at -1.32 V vs. RHE, which indicates that Pt/C is more likely to undergo HER reaction. The adsorption strength of hcp Ni NPs and fcc Ni NPs for acetone is weak, resulting in low catalyst conversion. Figure 6b clearly reveals the adsorption strength of isopropanol on the catalyst. When using hcp Ni NSs as the catalyst, a weak peak was observed at the hydroxyl group (-OH) (~ 3419.7 cm^{-1}), indicating that the desorption capacity of isopropanol to hcp Ni NSs was very strong. Therefore, the product isopropanol could quickly fall off after formation on the surface of the catalyst. For hcp Ni NPs, fcc Ni NPs and Pt/C, the absorption peak of hydroxyl group (-OH) (~ 3419.7 cm^{-1}) can be seen, indicating that isopropanol has a strong adsorption capacity on these catalysts, which makes it difficult for the isopropanol generated on the hcp Ni NPs, fcc Ni NPs and Pt/C surface to desorb quickly from their surface. This results in an unsatisfactory acetone conversion by hcp Ni NPs, fcc Ni NPs and Pt/C.

The free radical capture experiment was carried out by electron paramagnetic resonance (EPR) using 5, 5-dimethyl-1-pyrrolin-n-oxide (DMPO) as a free radical spin catcher. Only DMPO-H^* signal was captured in 1 M KOH electrolyte, after adding acetone to the electrolyte, the DMPO-H^* signal decreased significantly, suggesting that the surface-adsorbed hydrogen intermediates (H^*) were actively consumed in the hydrogenation reaction (Fig. 6c). This provides direct evidence for the involvement of H^* species in the electrocatalytic conversion of acetone. In order to explore the power and hydrogen source in the electrocatalytic hydrogenation reaction, the control experiments were carried out. These experiments confirm the necessity of electricity as the driving force and H_2O as the sole hydrogen source (Supplementary Fig. 40). The electrocatalytic acetone hydrogenation reaction was carried out by replacing H_2O with D_2O, and it was found that only deuterated isopropanol was produced by high-resolution mass spectrometry (HR-MS) (Supplementary Fig. 41), thus demonstrating that the H^* required for the hydrogenation process can only originate from the in-situ dissociation of H_2O[40].

To further understand the underlying mechanism of the enhanced activity for hcp Ni, DFT calculations were carried out. The acetone reduction (i.e. hydrogenation) is composed of acetone adsorption, followed by two steps of proton-coupled electron transfer (PCET) processes, and then desorption from active sites accordingly. As shown in Fig. 6d, the formation energy of key intermediate —— $^*C_3H_7O$ on the (0001) surface of hcp Ni, is slightly lower than that on the (111) surface of fcc Ni (0.18 vs 0.19 eV), combined with the desorption energy of isopropanol on hcp Ni is 0.07 eV lower than that on fcc Ni (Fig. 6e), indicating hydrogenation of acetone is thermodynamically favourable for hcp Ni. Moreover, considering H_2O as proton source, its adsorption and dissociation on active sites are also important factors for hydrogenation performance. As shown in Fig. 6f, the dissociation barrier of water molecule on the (0001) surface of hcp Ni is also lower by 0.02 eV than that on the (111) surface of fcc Ni, suggesting faster kinetics for water capture and dissociation over hcp Ni surface. Hence, the overall scenario of hydrogenation of acetone can be emphasized by the synergy of reduced product binding capacity and faster kinetics which is responsible for enhanced performance over hcp Ni catalysts.

To gain deeper insight into the origin of the high catalytic activity of hcp Ni NSs, quasi-in-situ ATR-IR spectroscopy was employed. Specifically, the acetone adsorption intensity on hcp Ni NSs increased markedly within the first 4 minutes of reaction (Fig. 6g, h), which is attributed to their higher specific surface area and the abundance of accessible active sites (Supplementary Figs. 42, 43 and Supplementary Notes 1, 2). In contrast, hcp Ni NPs exhibited a delayed increase in adsorption intensity, becoming significant only after 15 minutes (Fig. 6j, k), likely due to the relatively lower density of active sites accessible on their surface compared to the nanosheets. For fcc Ni NPs, a pronounced enhancement in acetone adsorption was observed only after 20 minutes (Fig. 6m, n), this may be attributed to the weak adsorption of acetone on the surface of fcc Ni NPs. In addition, the acetone adsorption intensity on the surface of Pt/C increased significantly at around 8 minutes (Supplementary Fig. 44), which may be attributed to the strong competitive HER reaction during the ECH of Pt/C.

Based on the above results, the possible reaction mechanisms of electrocatalytic acetone hydrogenation with H_2O over hcp Ni NSs, hcp Ni NPs and fcc Ni NPs are proposed (Fig. 6i, l, o). Acetone exhibits a high adsorption energy on hcp Ni NSs, enabling its rapid adsorption onto the catalyst surface. Concurrently, water molecules readily dissociate to release H^* on the surface, which subsequently participate in the electrocatalytic acetone hydrogenation, accompanied by the evolution of a small amount of hydrogen gas. Owing to the lower desorption energy of isopropanol on hcp Ni NSs compared to that on hcp Ni NPs and fcc Ni NPs, the isopropanol product is rapidly released from the catalyst surface. This facilitates the regeneration of active sites and promotes the continuous adsorption of acetone molecules, thereby sustaining a high catalytic turnover. In contrast, acetone exhibits relatively weak adsorption on fcc Ni NPs, leading to a slower surface reaction rate. Furthermore, the strong desorption energy of isopropanol on fcc Ni NPs results in the accumulation of products on the surface, which blocks active sites and further suppresses acetone conversion.

Discussion

In summary, we report two-dimensional metastable-phase Ni hexagonal nanosheets catalyst for efficient electrocatalytic acetone hydrogenation to isopropanol. Notably, the hcp Ni NSs exhibited acetone conversion of 95.9 ± 1.4%, isopropanol selectivity of 100 % and isopropanol production rate of 11.51 g g_{cat}^{-1} h^{-1} at -250 mA cm^{-2}. Quasi-in-situ ATR-IR and DFT calculations show that the hcp Ni NSs enable strong and rapid adsorption of acetone through its polar $C = O$ bond and rapid desorption of isopropanol. Additionally, the hcp Ni surface lowers the energy barrier for water dissociation, leading to faster generation of reactive H^* species. Furthermore, this catalyst has significant versatility for various carbonyl compounds. Our work not only provides a unique guide for the design of 2D metastable-phase electrocatalysts, but also provides a demonstration for the use of two-dimensional metastable-phase electrocatalysts with high catalytic activity for other electrochemical conversions besides electrocatalytic acetone hydrogenation.

Methods

Chemicals

Bis (η5-2,4-cyclopentadien-1-yl) nickel ($Ni(C_5H_5)_2$, 98%), nickel (II) oxalate dihydrate ($NiC_2O_4 \cdot 2H_2O$, 98%), ribose ($C_5H_{10}O_5$, 99%) deuterium oxide (D_2O, AR, 99%) and 2-heptanone ($C_7H_{14}O$, 98%) were

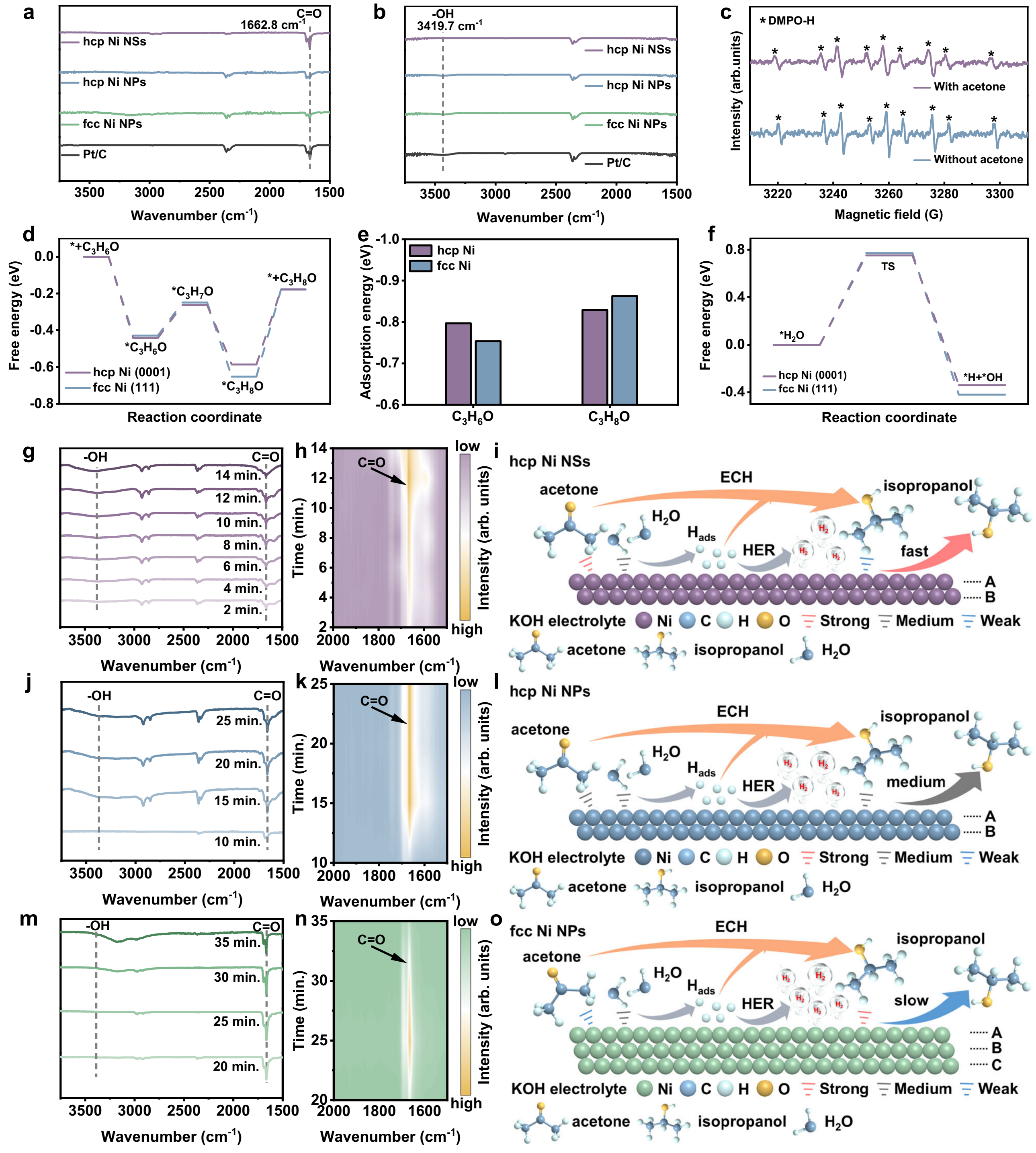

Fig. 6 | Mechanism exploration of ECH and density functional theory (DFT) calculation. a Infrared (IR) spectra of four catalysts treated with acetone (AC): hcp Ni NSs with AC, hcp Ni NPs with AC, fcc Ni NPs with AC and Pt/C with AC (from top to bottom). Infrared characteristic peak position of acetone carbonyl bond (C = O: 1662.8 cm^{-1}). **b** Infrared (IR) spectra of four catalysts treated with isopropanol (IPA): hcp Ni NSs with IPA, hcp Ni NPs with IPA, fcc Ni NPs with IPA and Pt/C with IPA (from top to bottom). Infrared characteristic peak position of hydroxyl bond (-OH: 3419.7 cm^{-1}) of isopropanol. **c** EPR result for electrocatalytic acetone hydrogenation in 1.0 M KOH/H_2O electrolyte over hcp Ni NSs. **d** Free energy profiles of acetone reduction pathway on hcp Ni and fcc Ni. **e** Adsorption energy of acetone and isopropanol on hcp Ni and fcc Ni, respectively. **f** Comparison of water dissociation on hcp Ni and fcc Ni. Quasi-in-situ ATR-IR spectroscopy and proposed reaction mechanisms for electrocatalytic acetone hydrogenation of **(g, h, i)** hcp Ni NSs, **(j, k, l)** hcp Ni NPs and **(m, n, o)** fcc Ni NPs.

purchased from Aladdin Industrial Corporation. Oleylamine ($CH_3(CH_2)_7CH = CH(CH_2)_7CH_2NH_2$, OAm, 68–70%) and nickel (II) acetylacetonate (Ni(acac)$_2$, 96%) were purchased from J&K Scientific Ltd. Nickel (II) formate dihydrate (Ni $(HCO_2)_2{\cdot}2H_2O$, 95%) and dibromobis (triphenylphosphine) nickel (II) ($NiBr_2(PPh_3)_2$, 98%) were purchased from Alfa Aesar. Glucose ($C_6H_{12}O_6$, AR), cyclohexane (C_6H_{12}, ≥ 99.5%), ethanol (C_2H_6O, 95.0%), isopropanol (C_3H_8O, ≥ 98.5%), formaldehyde (CH_2O, AR, Shanghai, China), 2-butanone (C_4H_8O, AR), 3-pentanone ($C_5H_{10}O$, ≥ 98%), cyclohexanone ($C_6H_{10}O$, AR), dichloromethane (CH_2Cl_2, AR) and potassium hydroxide (KOH, 95.0–98.0%) were purchased from Sinopharm Chemical Reagent Co., Ltd. (Shanghai, China). Nafion solution (~5 wt%, a mixture of lower aliphatic alcohols and water) was purchased from Sigma-Aldrich. Acetone (C_3H_6O, AR) was purchased from Chinasun Specialty Products Co., Ltd. (Jiangsu, China). Dimethyl sulfoxide-d6 (DMSO-d_6, 99.9%) and Raney Nickel (Ni, AR) were purchased from Energy Chemical. 2-Pentanone ($C_5H_{10}O$, > 99.0%), 3-heptanone ($C_7H_{14}O$, > 98.0%), cyclopentanone (C_5H_8O, > 99.0%) and benzophenone ($C_{13}H_{10}O$, > 99.0%) were purchased from TCI. 2-Hexanone ($C_6H_{12}O$, 98%) was purchased from Adamas. Cycloheptanone ($C_7H_{12}O$, 99%), cyclooctanone ($C_8H_{14}O$, 97%) and 2-indanone (C_9H_8O, 98%) were purchased from Acmec. 3-Hexanone ($C_6H_{12}O$, 98%) and 4-heptanone ($C_7H_{14}O$, 98%) were purchased from Shanghai Macklin Biochemical Technology Co., Ltd. Acetophenone (C_8H_8O, 98%) was purchased from Accela ChemBio Co. Ltd. (Shanghai, China). Commercial Pt/C (with noble metal loading of 20 wt%) was purchased from Johnson Matthey (JM). 5,5-Dimethyl-1-pyrroline N-oxide (DMPO, ≥ 98%) was purchased from Beijing Solarbio Science & Technology Co., Ltd. All the chemicals were used without further purification. The FAB-PK-130 anion 11 exchange membrane was purchased from Suzhou Yilongsheng Energy Technology Co. Ltd. The de-ionized water (18 MΩ cm^{-1}) used in all experiments was prepared by passing water through an ultra-pure purification system (Aqua Solutions).

Syntheses of hcp Ni NSs

Firstly, 9.4 mg of bis (η5-2,4-cyclopentadien-1-yl) nickel, 60 mg of glucose, 100 µL of formaldehyde, and 5.0 mL of oleylamine ($CH_3(CH_2)_7CH = CH(CH_2)_7CH_2NH_2$, OAm, 68–70%) were mixed and added to a glass bottle (volume 35 mL), which was placed in an ultrasonic machine for ultrasonic treatment for about 2 h. Then, the resulting homogeneous mixture was heated from ambient temperature to 210 °C in an oil bath at the heating rate of 5 °C per minute and maintained for 5 h. After the mixture was cooled to ambient temperature naturally, the resulting product was collected, washed, and centrifuged three times through a cyclohexane/ethanol mixture.

Syntheses of hcp Ni NPs and fcc Ni NPs

Nickel (II) acetylacetonate (Ni(acac)$_2$) (12.8 mg), glucose (60 mg) and OAm (5.0 mL) were added into a glass vial (volume: 35 mL). After the vial had been capped, the mixture was ultrasonicated for around 2 h. The resulting homogeneous mixture was then heated from ambient temperature to 230 °C for 5 h in an oil bath pan. After it was cooled to ambient temperature, the resulting products were collected by centrifugation and washed three times with a cyclohexane/ethanol mixture. The similar procedure was adopted for the preparation of fcc Ni NPs except adding glucose.

Characterizations

Low-magnification transmission electron microscopy (TEM) images were collected on a Hitachi HT7700 transmission electron microscope with the accelerating voltage of 120 kV. The crystal nanostructures were analyzed by an X-ray powder diffraction (XRD, X'Pert-Pro MPD diffractometer) equipped with a Cu Kα radiation source (λ = 0.15406 nm). The high-resolution TEM (HRTEM), energy dispersive spectroscopy (EDS) and EDS elemental mapping were achieved by FEI Tecnai F20 TEM at an accelerating voltage of 200 kV. X-ray photoelectron spectroscopy (XPS) spectra were collected with an SSI S-Probe XPS spectrometer. XAS data were collected at the TPS44 beamline of the National Synchrotron Radiation Research Center (NSRRC, Hsinchu, Taiwan), respectively. Data were processed according to standard procedures using the Demeter program package (Version 0.9.24). The liquid products were test by ^1H NMR (Aligent DD2-600, BRUKER AVANCE NEO 400 MHz and BRUKER AVANCEIII HD-400) spectrometer. Attenuated total reflectance infrared (ATR-IR) spectra was recorded on a Bruker Vertex 70 spectrometer in the spectral range of 4000 cm^{-1} to 600 cm^{-1}. Hydrogen and radicals were investigated via electron paramagnetic resonance (EPR) spectroscopy (JES-X320, Japan). High-Resolution mass spectrometry (HR-MS) was recorded on a Bruker micrOTOF-Q III.

The preparation of catalysts for electrochemical of characterizations

5 mg of catalyst was dispersed in 500 µL ethanol and 10 µL of 5 wt% Nafion by sonication for 30 minutes to form a homogeneous ink. Then the homogeneous catalyst ink was dropped evenly on carbon paper (CP, loading area 1.0 cm^2) as the working electrode. The catalysts used in this experiment were all loaded onto 1.0 cm^2 carbon paper and used as the working electrode, with a loading of 5 mg cm^{-2}, unless otherwise specified. catalyst loading = m (catalyst amount) / s (area of carbon paper).

Electrochemical characterization

The electrochemical measurements were carried out on CHI 660E workstation. All the experiments were carried out at room temperature. All electrolytes used in the tests were freshly prepared and used immediately. 1.0 M KOH/H_2O electrolyte was prepared by dissolving KOH solid powder in deionized water, the pH of the 1 M KOH electrolyte is 13.7 ± 0.3. The electrochemical measurements were carried out in a divided two-compartment electrochemical cell consisting of a working electrode, a carbon rod counter electrode, and a saturated calomel electrode as the reference electrode. The cathode cell (10 mL) and anode cell (10 mL), respectively, containing 1.0 M KOH/H_2O electrolyte (7 mL) were separated by an untreated Nafion 211 proton exchange membrane (size: 2 × 2 cm^2, thickness: 25 mm). 0.1 mmol acetone dissolving in 1.0 M KOH/H_2O electrolyte (7 mL) was added into the cathode cell and stirred to form a homogeneous solution. Then, chronoamperometry was carried out under stirring (750 rpm). After the reactions were finished, the solution at the cathode cell was extracted with dichloromethane and tested using ^1H NMR to calculate the acetone conversion (con.) and the isopropanol selectivity (sel.). For scaled-up experiment, The electrolysis was carried out in a flow electrolysis cell with Ni foam with a working area of 1 cm^2 as the anode, hcp Ni NSs with a working area of 1 cm^2 as the cathode, 1.0 M KOH/H_2O electrolyte (10 mL) containing 20 mmol acetone as the catholyte, 1.0 M KOH/H_2O electrolyte (10 mL) as the anolyte, and a flow rate of the cathode and anolyte of 235 mL min^{-1}. The cathodic and anodic blocks were separated by an anion exchange membrane. In this work, conversion (con.) is referred to as acetone substrates, and selectivity (sel.) is referred to as isopropanol products. The acetone conversion (con.) and isopropanol selectivity (sel.) were calculated using Eqs. (1) - (2) below.

$$Con.(\%) = \frac{n\,(\text{consumed}\quad\text{acetones})}{n\,(\text{initial}\quad\text{acetones})} \times 100\% \tag{1}$$

$$Sel.(\%) = \frac{n\,(\text{obtained}\quad\text{isopropanol})}{n\,(\text{consumed}\quad\text{acetones})} \times 100\% \tag{2}$$

The production rate and reaction rate were calculated as follows:

$$Production\ Rate\,(\mathrm{g\,g_{cat}^{-1}\,h^{-1}}) = \frac{m\,(\text{mass of obtained isopropanol})}{m\,(\text{mass of the catalyst}) \times t\,(\text{reaction time})} \tag{3}$$

$$Reaction\ Rate\,(\mu\mathrm{mol\,cm^{-2}\,h^{-1}}) = \frac{n\,(\text{obtained isopropanol})}{s\,(\text{area of carbon paper}) \times t\,(\text{reaction time})} \tag{4}$$

The Faradaic efficiency (FE) was obtained according to the following equation:

$$FE = \frac{2nF}{It} \times 100\% \tag{5}$$

Where *F* is the Faraday constant (96485 C mol^{-1}), *n* is the number of moles of the produced isopropanol, *I* is the current (A) and *t* is the reaction time (s).

In ^{1}H NMR spectra, when using DMSO-d$_6$ as the solvent for NMR tests, the peaks at 2.5 ppm and 3.3 ppm were assigned to the hydrogen signal of DMSO-d$_6$ and H_2O.

All potentials in this work were referenced to $Hg/HgCl_2$. The reversible hydrogen electrode (RHE) is suitable for electrolytes containing 1.0 M KOH. The reference electrode calibration steps are as follows: Using one Pt wire as the working electrode and the other Pt wire as the counter electrode, LSV tests were performed on a saturated calomel electrode in the highly pure H_2-saturated 1.0 M KOH electrolyte at a scan rate of 1 mV s^{-1}. The calibration value of the reference electrode is −1.01 V vs. SCE. All potentials measured were calibrated to RHE using the following equation:

$$E\,(\mathrm{RHE}, 1.0\mathrm{M\,KOH}) = E\,(\mathrm{SCE}) + 1.01\,\mathrm{V} \tag{6}$$

LSV was recorded without *iR* correction to obtain the polarization curves. Then, chronoamperometry was carried out at a given constant potential. Electrochemical double-layer (C_{dl}) was carried out by CV in the potential range of 0.65 ~ 0.85 V vs. RHE with a scanning rate of 20, 40, 60, 80, 100, 120, 140, 160, 180 and 200 mV/s. The Δj/2 obtained at 0.75 V vs. RHE was plotted against the scan rate, and the fitted slope was the measured C_{dl} value. The Electrochemical Impedance Spectroscopy (EIS) experiment steps are as follows: 5 mg of catalyst was dispersed in 500 μL ethanol and 10 μL of 5 wt% Nafion by sonication for 30 minutes to form a homogeneous ink. A 15 μL homogeneous ink was dropped on the surface of the GCE (5 mm in diameter) and dried naturally, which was the modified GCE as the working electrode. A saturated calomel electrode and a carbon rod (cylind rical carbon material with 3 mm in diameter and 5 cm in length) were used as the reference electrode and counter electrode, respectively. The test was conducted at the potential corresponding to a current density of −10 mA cm^{-2}.

EPR experiments for electrochemical hydrogenation of acetone

The hcp Ni NSs working electrode and reference electrode were implanted in the cathode chamber, and the graphite rod pair electrode was implanted in the anode chamber. Chronoamperometry was performed at 0.1 mmol acetone or no 0.1 mmol acetone for 10 minutes at a given constant potential of −1.32 V vs. RHE in 1.0 M KOH/H_2O (7.0 mL). Then add 0.1 mmol of 5, 5-dimethyl-1-pyrrolin-n-oxide (DMPO) dissolved in 1.0 M KOH/H_2O electrolyte, stirring for 1 minute, and quickly remove it for EPR test.

Quasi-in-situ ATR-IR measurements

First of all, the Quasi-in-situ FTIR spectra testing method is listed as follows. The catalyst ink is dropped onto a glassy carbon electrode and then dried. In a divided two-compartment electrochemical cell, we add 0.1 mmol acetone in 1.0 M KOH/H_2O (7 mL) electrolyte and apply the voltage of −1.32 V vs. RHE to the working electrode for different time. Finally, the catalyst on the glassy carbon electrode was collected by ultrasound in an ethanol solution for liquid FTIR spectra testing.

Computational details

Ab initio quantum mechanical (QM) calculations were performed using the Vienna Ab initio Simulation Package (VASP), version 5.4.4, employing the projector augmented wave (PAW) method with a plane-wave basis set. The electronic structure was described within the framework of density functional theory (DFT, Supplementary Data 1) using the generalized gradient approximation (GGA) of the Perdew-Burke-Ernzerhof (PBE) functional[41–43]. Dispersion corrections were incorporated via the DFT-D3 method with Becke-Jonson damping[44]. A plane-wave energy cutoff of 400 eV was used, as benchmark tests indicated that a higher cutoff did not improve accuracy. Integration over the Brillouin zone was performed using a Γ-centered 3 × 3 × 1 Monkhorst-Pack k-point grid. Finer k-point spacing did not yield more accurate predictions. Partial orbital occupancies were treated using the first-order Methfessel-Paxton scheme with a smearing width of 0.2 eV. Dipole moment corrections were applied along the surface normal direction. Self-consistent field (SCF) iterations were considered converged when the change in total energy and eigenvalues between successive steps both fell below 1×10^{-6} eV. Ionic relaxation was carried out using a conjugate-gradient algorithm until all atomic forces were below 0.01 eV/Å. The resulting geometries were confirmed as energy minima through vibrational frequency analysis, ensuring the absence of imaginary frequencies. The Hessian matrix, required for frequency calculations, was obtained via finite-difference displacements of ± 0.04 Å along each Cartesian direction for each ion. In these calculations, only the adsorbed species were displaced while the slab atoms remained fixed. All computations were performed under standard conditions of 298 K and 1 bar. Free energies were calculated using standard statistical mechanical expressions accounting for translational, rotational, vibrational, and electronic contributions[45]. For surface-adsorbed species, translational and rotational contributions to the free energy were omitted. The partition function under the harmonic oscillator approximation is as follows:

$$q_{vib} = \prod_i \frac{e^{-\frac{h\upsilon_i}{2kT}}}{1 - e^{-\frac{h\upsilon_i}{kT}}} \tag{7}$$

where k is a force constant, ν is the vibrational frequency, after substituting the partition function q_{vib}, the internal energy correction is as follows:

$$U_{vib}(\mathrm{T}) = R\sum_{\mathrm{i}}\left(\frac{h\upsilon_i}{k}\right)\left(\frac{1}{2} + \frac{e^{-\frac{h\upsilon_i}{kT}}}{1 - e^{-\frac{h\upsilon_i}{kT}}}\right) \tag{8}$$

The first term is the contribution of zero-point energy (ZPE), and the second term is the contribution of internal energy correction from 0 K to 298 K. The correction of entropy (S) is as follows:

$$S_{vib}(\mathrm{T}) = R\sum_{\mathrm{i}}\left\{\frac{h\upsilon_i}{kT}\frac{e^{-\frac{h\upsilon_i}{kT}}}{1 - e^{-\frac{h\upsilon_i}{kT}}} - ln\left[1 - e^{-\frac{h\upsilon_i}{kT}}\right]\right\} \tag{9}$$

Here, the first term exactly cancels with the second term of the internal energy shown above. Therefore, only the second term of the entropy needs to be corrected. For adsorbed species, the six degrees of freedom of the translation and rotation are frustrated and considered vibration. Such approximation fails when the vibration is extremely low that has a significant contribution to the correction. To avoid such overestimation, the contribution of frequencies below 50 cm^{-1} are all considered as 50 cm^{-1}.

Zero-point energy (ZPE) in thermo energy correction is as follows:

$$\varepsilon_{ZPE} = \frac{h\nu}{2} \tag{10}$$

The Gibbs free energy G can be derived as follows:

$$G = E_{ZPE} + E + k_B T - TS \tag{11}$$

The above correction is obtained by using VASPKIT code for a post-processing of the VASP output data[46]. While the DFT results provide insights into adsorption and reaction pathways, there are many difficulties in accurately simulating the material under catalytic conditions, and it may not fully represent the real catalytic interface under electrochemical conditions, thus having certain limitations.

Data availability

The data generated in this study are provided in the Supplementary Information/Source Data file. Source data are provided with this paper.

References

1. Lin, J. et al. Efficient electroreduction of carbonyl compounds to alcohols over Fe/Fe_2O_3 interfaces. *Nat. Catal.* **8**, 338–347 (2025).
2. Genest, A. et al. The origin of the particle-size-dependent selectivity in 1-butene isomerization and hydrogenation on Pd/Al_2O_3 catalysts. *Nat. Commun.* **12**, 6098 (2021).
3. Guo, M. et al. The promotion effect of π-π interactions in Pd NPs catalysed selective hydrogenation. *Nat. Commun.* **13**, 1770 (2022).
4. Wang, L. et al. Single-site catalyst promoters accelerate metal-catalyzed nitroarene hydrogenation. *Nat. Commun.* **9**, 1362 (2018).
5. Zhang, Z. et al. Electrocatalytic aromatic alcohols splitting to aldehydes and H_2 gas. *J. Am. Chem. Soc.* **146**, 27179–27185 (2024).
6. Xu, M. et al. Selective cleavage of α-olefins to produce acetylene and hydrogen. *J. Am. Chem. Soc.* **146**, 12850–12856 (2024).
7. Shen, M. et al. Ni-foam-structured Ni-Al_2O_3 ensemble as an efficient catalyst for gas-phase acetone hydrogenation to isopropanol. *ACS Appl. Mater. Interfaces* **13**, 28334–28347 (2021).
8. Ji, Y. et al. Porous bimetallic Pt-Fe nanocatalysts for highly efficient hydrogenation of acetone. *Nano Res.* **8**, 2706–2713 (2015).
9. Ro, I. et al. Intrinsic activity of interfacial sites for Pt-Fe and Pt-Mo catalysts in the hydrogenation of carbonyl groups. *Appl. Catal. B: Environ.* **231**, 182–190 (2018).
10. Gao, X. et al. Microkinetic analysis of acetone hydrogenation over Pt/SiO_2. *J. Catal.* **374**, 183–198 (2019).
11. Qin, R. et al. Alkali ions secure hydrides for catalytic hydrogenation. *Nat. Catal.* **3**, 703–709 (2020).
12. Wang, X. et al. Insights into the shape effect of H_2 self-selective Ni catalysts for efficient acetone hydrogenation. *Appl. Surf. Sci.* **536**, 147844 (2021).
13. Özkar, S. & Finke, R. G. Iridium(0) nanocluster, acid-assisted catalysis of neat acetone hydrogenation at room temperature: exceptional activity, catalyst lifetime, and selectivity at complete conversion. *J. Am. Chem. Soc.* **127**, 4800–4808 (2005).
14. Yang, H., Goldbach, A. & Shen, W. Acetone hydrogenation over face-centered cubic and hexagonal close-packed cobalt. *Int. J. Hydrog. Energy* **51**, 1360–1372 (2024).
15. Liu, K. et al. Intensified gas-phase hydrogenation of acetone to isopropanol catalyzed at metal-oxide interfacial sites. *Chem. Eng. J.* **454**, 140059 (2023).
16. Xia, Z. et al. Enhancing the electrocatalytic hydrogenation of furfural via anion-induced molecular activation and adsorption. *J. Am. Chem. Soc.* **146**, 24570–24579 (2024).
17. Xu, W. et al. Electrochemical hydrogenation of biomass-based furfural in aqueous media by Cu catalyst supported on *N*-doped hierarchically porous carbon. *Appl. Catal. B: Environ.* **305**, 121062 (2022).
18. Liu, W. et al. High-efficiency electrochemical hydrodeoxygenation of bio-phenols to hydrocarbon fuels by a superacid-noble metal particle dual-catalyst system. *Energy Environ. Sci.* **13**, 917–927 (2020).
19. Zhao, Z. et al. Heteroatom introduction and electrochemical reconstruction on heterostructured Co-based electrocatalysts for hydrogenation of quinolines. *Small* **21**, 2412626 (2025).
20. Liu, Y. et al. Layered double hydroxide-derived Ni-Cu nanoalloy catalysts for semi-hydrogenation of alkynes: improvement of selectivity and anti-coking ability via alloying of Ni and Cu. *J. Catal.* **359**, 251–260 (2018).
21. Golubina, E. V. et al. The role of metal–support interaction in catalytic activity of nanodiamond-supported nickel in selective phenylacetylene hydrogenation. *J. Catal.* **344**, 90–99 (2016).
22. Bridier, B. & Pérez-Ramírez, J. Cooperative effects in ternary Cu-Ni-Fe catalysts lead to enhanced alkene selectivity in alkyne hydrogenation. *J. Am. Chem. Soc.* **132**, 4321–4327 (2010).
23. Yu, J.-W. et al. Synthesis of ultrathin Ni nanosheets for semihydrogenation of phenylacetylene to styrene under mild conditions. *Nanoscale* **10**, 6936–6944 (2018).
24. Peng, T. et al. Ternary alloys enable efficient production of methoxylated chemicals via selective electrocatalytic hydrogenation of lignin monomers. *J. Am. Chem. Soc.* **143**, 17226–17235 (2021).
25. Yu, H. et al. Strain-triggered distinct oxygen evolution reaction pathway in two-dimensional metastable phase IrO_2 via CeO_2 loading. *J. Am. Chem. Soc.* **146**, 20251–20262 (2024).
26. Liao, F. et al. Iridium oxide nanoribbons with metastable monoclinic phase for highly efficient electrocatalytic oxygen evolution. *Nat. Commun.* **14**, 1248 (2023).
27. Zhang, J. et al. Atomic-thick metastable phase RhMo nanosheets for hydrogen oxidation catalysis. *Nat. Commun.* **14**, 1761 (2023).
28. Li, Z. et al. 1 T'-transition metal dichalcogenide monolayers stabilized on 4H-Au nanowires for ultrasensitive SERS detection. *Nat. Mater.* **23**, 1355–1362 (2024).
29. Ge, Y. et al. Two-dimensional nanomaterials with unconventional phases. *Chem* **6**, 1237–1253 (2020).
30. Zhou, X. et al. Preparation of Au@Pd core–shell nanorods with fcc-2H-fcc heterophase for highly efficient electrocatalytic alcohol oxidation. *J. Am. Chem. Soc.* **144**, 547–555 (2022).
31. Fan, Z. et al. Heterophase fcc-2H-fcc gold nanorods. *Nat. Commun.* **11**, 3293 (2020).
32. Wang, C. et al. NiFe alloy nanoparticles with hcp crystal structure stimulate superior oxygen evolution reaction electrocatalytic activity. *Angew. Chem. Int. Ed.* **58**, 6099–6103 (2019).
33. Fang, M. et al. Metastable metal-alloy interface in RuNi nanoplates boosts highly efficient hydrogen electrocatalysis. *ACS Appl. Nano Mater.* **5**, 17496–17502 (2022).
34. Su, J. et al. Core-shell design of metastable phase catalyst enables highly-performance selective hydrogenation. *Adv. Mater.* **36**, 2308839 (2024).
35. Zhan, C. et al. Subnanometer high-entropy alloy nanowires enable remarkable hydrogen oxidation catalysis. *Nat. Commun.* **12**, 6261 (2021).
36. Wang, L. et al. Stabilizing low-valence single atoms by constructing metalloid tungsten carbide supports for efficient hydrogen oxidation and evolution. *Angew. Chem. Int. Ed.* **62**, e202311937 (2023).
37. Liu, S. et al. Ultrathin perovskite derived Ir-based nanosheets for high-performance electrocatalytic water splitting. *Energy Environ. Sci.* **15**, 1672–1681 (2022).
38. Xu, Y.-F. et al. High-performance light-driven heterogeneous CO_2 catalysis with near-unity selectivity on metal phosphides. *Nat. Commun.* **11**, 5149 (2020).
39. Tian, T. et al. Study of the active sites in porous nickel oxide nanosheets by manganese modulation for enhanced oxygen evolution catalysis. *ACS Energy Lett.* **3**, 2150–2158 (2018).
40. Wu, Y. et al. Converting copper sulfide to copper with surface sulfur for electrocatalytic alkyne semi-hydrogenation with water. *Nat. Commun.* **12**, 3881 (2021).
41. Grimme, S., Ehrlich, S. & Goerigk, L. Effect of the damping function in dispersion corrected density functional theory. *J. Comput. Chem.* **32**, 1456–1465 (2011).
42. Dong, T. et al. Lattice and surface engineering of ruthenium nanostructures for enhanced hydrogen oxidation catalysis. *Adv. Funct. Mater.* **33**, 2210328 (2022).
43. Zhu, W. et al. Boosting the acidic water oxidation activity by an interfacial oxygen migration in rutile-1T-heterophase IrO_2 catalysts. *Nano Energy* **131**, 110280 (2024).
44. Perdew, J. P., Burke, K. & Ernzerhof, M. Generalized gradient approximation made simple. *Phys. Rev. Lett.* **77**, 3865–3868 (1996).

45. McQuarrie D. A. Statistical Mechanics. University Science Books. (2000).
46. Wang, V. et al. VASPKIT: a user-friendly interface facilitating high-throughput computing and analysis using VASP code. *Comput. Phys. Commun.* **267**, 108033 (2021).

Acknowledgements

This work was financially supported by the Ministry of Science and Technology of China (2024YFA1509500 to Q.S.), National Natural Science Foundation of China (22475143 to Q.S.), the Jiangsu Natural Science Fund for Distinguished Young Scholars (BK20250047 to Q.S.), Young Elite Scientists Sponsorship Program by CAST (grant no. 2023QNRC001 to Q.S.), the Priority Academic Program Development of Jiangsu Higher Education Institutions (PAPD) and Collaborative Innovation Center of Suzhou Nano Science and Technology.

Author contributions

Q.S. conceived and supervised the experiments. L.C. and Q.S. wrote the paper. Z.Z. and H.Y. performed the DFT calculation. L.C. and Q.S. carried out the majority of the research and data result analysis. P.L. and L.C. performed the material characterization combining TEM/HRTEM. L.C., H.L., C.L. and S.P. performed the material characterization. W.H., C.P. and Z.H. performed the XAS characterization. All authors discussed the results and commented on the manuscript.

Competing interests

The authors declare no competing interests.

Additional information

Supplementary information The online version contains supplementary material available at https://doi.org/10.1038/s41467-025-67839-6.

Correspondence and requests for materials should be addressed to Qi Shao.

Peer review information *Nature Communications* thanks Xiaoming Sun, Yao Zheng, Pan Liu and the other, anonymous, reviewer(s) for their contribution to the peer review of this work. A peer review file is available.

Reprints and permissions information is available at http://www.nature.com/reprints